RESEARCH ARTICLE

Cryo-electron microscopy structures of the N501Y SARS-CoV-2 spike protein in complex with ACE2 and 2 potent neutralizing antibodies

Xing Zhu[1]⊙, Dhiraj Mannar[1]⊙, Shanti S. Srivastava[1]⊙, Alison M. Berezuk[1]⊙, Jean-Philippe Demers[1], James W. Saville[1], Karoline Leopold[1], Wei Li[2], Dimiter S. Dimitrov[2], Katharine S. Tuttle[1], Steven Zhou[1], Sagar Chittori[1], Sriram Subramaniam[1]*

1 Department of Biochemistry and Molecular Biology, University of British Columbia, Vancouver, British Columbia, Canada, 2 Center for Antibody Therapeutics, Division of Infectious Diseases, Department of Medicine, University of Pittsburgh Medical School, Pittsburgh, Pennsylvania, United States of America

⊙ These authors contributed equally to this work.
* sriram.subramaniam@ubc.ca

Abstract

The recently reported "UK variant" (B.1.1.7) of SARS-CoV-2 is thought to be more infectious than previously circulating strains as a result of several changes, including the N501Y mutation. We present a 2.9-Å resolution cryo-electron microscopy (cryo-EM) structure of the complex between the ACE2 receptor and N501Y spike protein ectodomains that shows Y501 inserted into a cavity at the binding interface near Y41 of ACE2. This additional interaction provides a structural explanation for the increased ACE2 affinity of the N501Y mutant, and likely contributes to its increased infectivity. However, this mutation does not result in large structural changes, enabling important neutralization epitopes to be retained in the spike receptor binding domain. We confirmed this through biophysical assays and by determining cryo-EM structures of spike protein ectodomains bound to 2 representative potent neutralizing antibody fragments.

Introduction

The rapid international spread of severe acute respiratory syndrome coronavirus 2 (SARS-CoV-2), the causative agent of COVID-19, is associated with numerous mutations that alter viral fitness. Mutations have been documented in all 4 structural proteins encoded by the viral genome including the small envelope glycoprotein (E), membrane glycoprotein (M), nucleocapsid (N) protein, and the spike (S) protein. The most prominent mutations are in the spike protein, which mediates entry of the virus into cells by engaging with the angiotensin converting enzyme 2 (ACE2) receptor. Several structures of SARS-CoV-2 spike protein variants in pre- and post-fusion conformations have been reported, including complexes with ACE2 and a variety of antibodies [1–13]. Mutations that emerge in the receptor binding domain (RBD) of the spike protein are especially of interest given their high potential to alter the kinetics and

Abbreviations: BLI, biolayer interferometry; cryo-EM, cryo-electron microscopy; RBD, receptor binding domain; SARS-CoV-2, severe acute respiratory syndrome coronavirus 2.

strength of the interaction of the virus with target cells. These mutations could also affect the binding of antibodies capable of binding and blocking engagement of the virus with ACE2.

In December 2020, new variants of SARS-CoV-2 carrying several mutations in the spike protein were documented in the UK (SARS-CoV-2 VOC202012/01) and South Africa (501Y.V2) [14,15]. Early epidemiological and clinical findings have indicated that these variants show increased transmissibility in the population [16]. Despite being phylogenetically distinct, a common feature of both the UK and South African variants is the mutation of residue 501 in the RBD from Asn to Tyr (N501Y). X-ray crystallography and cryo-electron microscopy (cryo-EM) structural studies have identified N501 as a key residue in the spike protein at the interface between RBD and ACE2 that is involved in critical contacts with several ACE2 residues [5,6,10,13]. Studies carried out in a mouse model before the identification of the new UK variant suggested that mutations of residue 501 could be linked to increased receptor binding and infectivity [17,18]. Understanding the impact of N501Y on antibody neutralization, ACE2 binding, and viral entry is therefore of fundamental interest in the efforts to prevent the spread of COVID-19.

Results

Visualization of Y501 in contact with ACE2

To understand the structural effects of the N501Y mutation on ACE2 binding, we expressed and purified spike (S) protein ectodomains with and without the N501Y mutation in Expi293F cells (S1 Fig), and conducted microscopy studies on the ACE2–spike complexes. A cryo-EM structure of the spike protein ectodomain with the N501Y mutation was obtained at an average resolution of approximately 2.8 Å (Table 1; S2 Fig). The structure shows no significant global changes in secondary or quaternary structure as a result of the mutation when compared to the previously published structure of the spike protein ectodomain with an Asn residue at position 501 (referred to here as the "unmutated" form; S3 Fig) [7].

Cryo-EM structural analysis of the complex formed between the N501Y spike protein ectodomain and the ACE2 receptor ectodomain provides a detailed glimpse of both the overall structure of the receptor and the binding interface between the RBD and ACE2 (Fig 1; S4 Fig). The ACE2 receptor is bound to the "up" position of the RBD (Fig 1A). The overall structure of the complex was determined at a global resolution of 2.9 Å. Local refinement of the RBD–ACE2 interface improves the local resolution at the binding interface to approximately 3.3 Å (Fig 1B), resulting in unambiguous delineation of the Y501 side chain and other residues in the vicinity (Fig 1C). The overall structure at the binding site is almost identical to that of the unmutated version (Fig 1D) [7], with the exception of local rearrangements that result in the aromatic ring of Y501 being accommodated in a cavity that is sandwiched between Y41 and K353 of the ACE2 receptor (Fig 1E). Y501 in the spike protein and Y41 in the ACE2 receptor form a perpendicular y-shaped π–π stacking interaction [19].

Potent neutralization of SARS-CoV-2 has been achieved with a number of antibodies, including 2 recently reported examples, V_H Fc ab8 and IgG ab1, both derived from a large human library of antibody sequences [20,21]. We compared the efficiencies of these 2 antibodies, as well as the ACE2 receptor ectodomain, to bind spike proteins with and without the N501Y mutation. We also determined the relative efficiency of neutralization of pseudoviruses expressing either the N501Y mutant or unmutated form of the spike protein.

The N501Y mutation confers increased ACE2 binding affinity

To test the influence of the N501Y mutation on ACE2 binding, we used a luciferase reporter to measure the infectivity of pseudotyped viruses presenting N501Y or unmutated spike proteins for cells overexpressing ACE2 (S5 Fig). The higher relative luminescence unit (RLU) intensity

Table 1. Data collection and processing parameters, refinement and validation statistics.

Structure	S(N501Y)	S(N501Y) + V$_H$ ab8	S(N501Y) + V$_H$ ab8 focused refinement	S(N501Y) + Fab ab1 class 1	S(N501Y) + Fab ab1 class 2	S(N501Y) + Fab ab1 focused refinement	S(N501Y) + ACE2	S(N501Y) + ACE2 focused refinement
EMDB ID	23872	23873	23874	23875	23876	23877	23878	23879
PDB ID	7MJG	7MJH	7MJI	7MJJ	7MJK	7MJL	7MJM	7MJN
Data collection								
Microscope	Titan Krios G4	Titan Krios G4		Titan Krios G4			Titan Krios G4	
Detector	Falcon4	Falcon4		Falcon4			Falcon4	
Voltage (kV)	300	300		300			300	
Nominal magnification	155,000	155,000		155,000			155,000	
Defocus range (μm)	−3.0 to −0.5	−3.0 to −0.5		−3.0 to −0.5			−3.0 to −0.5	
Physical pixel (Å)	0.5	0.5		0.5			0.5	
Electron dose (e$^-$/Å^2)	40	40		40			40	
Exposure rate (e$^-$/Å^2/s)	24	24		24			24	
Format of movies	EER	EER		EER			EER	
Number of raw frames	399	399		399			399	
Number of movies	6,444	8,520		14,365			16,826	
Data processing								
Fractions (n)	40	40		40			40	
Extracted particles (n)	613,271	1,126,516		1,076,444			1,742,590	
Refined particles (n)	264,295	486,767		317,385			652,050	
Particles for final map (n)	205,360	208,633	229,078	66,865	124,227	372,681*	194,473	194,473
Symmetry imposed	C1	C1	C1	C1	C3	C1	C1	C1
Resolution (Å)	2.81	2.66	2.81	3.32	2.73	2.95	2.83	3.29
FSC threshold	0.143	0.143	0.143	0.143	0.143	0.143	0.143	0.143
Refinement								
Initial model used	6XKL	6XKL, 6WGJ	6XKL, 6WGJ	6XKL, 7CH5	6XKL, 7CH5	6XKL, 7CH5	6XKL, 7KNH	7KMB
Map sharpening B-factor (Å^2)	77.5	67.0	75.9	71.9	77.7	71.2	73.6	79.8
Composition (n)								
Atoms	25,260	28,146	2,523	31,680	34,878	4,788	35,096	6,526
Residues	3,120	3,495	320	3,968	4,389	621	4,312	797
Ligands	NAG:60	NAG:60	NAG:1	NAG:60	NAG:60	NAG:1	NAG:68	NAG:5
Overall B-factor (Å^2)								
Protein (min/max/mean)	76.52/393.91/150.44	53.79/789.22/180.32	66.00/120.86/88.80	78.57/473.81/213.31	63.46/398.30/182.55	82.02/163.62/109.04	52.13/765.11/260.03	71.02/292.02/150.49
Ligand (min/max/mean)	101.88/290.34/159.33	75.98/545.80/144.09	111.89/111.89/111.89	114.41/297.05/179.53	86.49/184.58/124.12	104.21/104.21/104.21	80.23/691.69/197.72	155.85/197.43/176.55
Bonds (RMSD)								
Length (Å) (n > 4σ)	0.004 (0)	0.004 (0)	0.006 (0)	0.004 (0)	0.004 (0)	0.005 (0)	0.004 (0)	0.004 (0)
Angles (°) (n > 4σ)	0.738 (7)	0.735 (9)	0.802 (0)	0.735 (8)	0.777 (6)	0.841 (1)	0.755 (6)	0.834 (3)
CC_mask	0.82	0.82	0.84	0.81	0.82	0.87	0.79	0.85
Validation								
Ramachandran plot								
Residues favored (%)	97.90	97.04	97.15	96.80	96.97	96.08	97.35	97.60
Residues disallowed (%)	0.00	0.00	0.00	0.00	0.00	0.00	0.00	0.00
Rotamer outliers (%)	0.00	0.00	0.00	0.00	0.00	0.00	0.00	0.00

(Continued)

Table 1. (Continued)

Structure	S(N501Y)	S(N501Y) + V_H ab8	S(N501Y) + V_H ab8 focused refinement	S(N501Y) + Fab ab1 class 1	S(N501Y) + Fab ab1 class 2	S(N501Y) + Fab ab1 focused refinement	S(N501Y) + ACE2	S(N501Y) + ACE2 focused refinement
Clash score	2.77	3.37	2.85	3.20	2.87	2.66	2.96	3.30
MolProbity score	1.21	1.30	1.23	1.31	1.25	1.32	1.21	1.20

*Derived after C3 symmetry expansion of 124,227 particles.

EER, electron event registration; FSC, Fourier shell correlation; RMSD, root-mean-square deviation.

from cells infected by the N501Y mutant (6,000 ± 2,000 RLU, mean ± standard deviation) compared to control viruses expressing the unmutated form (3,000 ± 800 RLU) suggests that the N501Y mutation may result in increased infectivity, assuming equal incorporation of spike proteins within the pseudotyped particles utilized. This finding is in agreement with a recent report demonstrating increased cell entry of pseudoviral particles incorporating the N501Y and D614G mutations relative to D614G alone [22]. To investigate whether the N501Y mutation increases the binding strength of the SARS-CoV-2 spike to ACE2, we measured the binding parameters between ACE2 and either unmutated or N501Y spike protein ectodomain trimers via biolayer interferometry (BLI). This revealed that the N501Y mutation confers a modest increase in affinity for ACE2, mainly driven by a reduction in the dissociation rate constant (k_{off}) (S5C and S5D Fig; S1 Table). Notably, several studies have demonstrated that the N501Y mutation confers much larger increases (3- to 16-fold) in ACE2 binding affinity when using minimal RBD constructs [23–28]. We also measured the efficiency of exogenously added soluble ACE2-mFc proteins to neutralize unmutated and N501Y pseudoviruses via pre-incubation prior to cell infection (S5B Fig). The comparison of neutralization profiles shows that the IC_{50} for neutralization of the N501Y mutant is lower, suggesting that full-length spikes bearing the N501Y mutation bind ACE2-mFc to a higher extent. Taken together with recent reports [22–28], these 3 results are consistent with the hypothesis that the greater infectivity of the N501Y mutant stems from improved binding to ACE2.

N501Y has minimal effects on the binding and potency of 2 neutralizing antibodies with RBD epitopes

Next, we tested the effect of the N501Y mutation on the relative strengths of binding and neutralization potency of V_H Fc ab8 and IgG ab1 (Fig 2). ELISA analysis of IgG ab1 and V_H Fc ab8 interactions with unmutated or N501Y spike ectodomains demonstrates that the N501Y mutation has no significant effect on V_H Fc ab8 binding but results in a slightly higher EC_{50} for IgG ab1 (Fig 2A; S1 Table). Second, competition experiments establish that IgG ab1 more efficiently prevents ACE2 binding of the unmutated ectodomain compared to the N501Y mutant (Fig 2C), while V_H Fc ab8 prevents ACE2 binding of unmutated and N501Y mutant spike proteins to similar extents (Fig 2D). This is further confirmed by negative stain experiments, where V_H ab8 interferes with ACE2 binding in both the unmutated and N501Y spikes (S6 Fig). Consistent with these measurements, neutralization experiments carried out with V_H Fc ab8 show that it can neutralize the N501Y mutant with a potency similar to that of the unmutated form, while IgG ab1 exhibits a slightly diminished neutralization potency for the N501Y mutant relative to pseudoviruses expressing the unmutated form (Fig 2B; S1 Table). Overall, binding and neutralization analyses show that the N501Y mutation results in enhanced ACE2 binding, minimal effects on the binding and potency of V_H Fc ab8, and a small reduction in the binding and
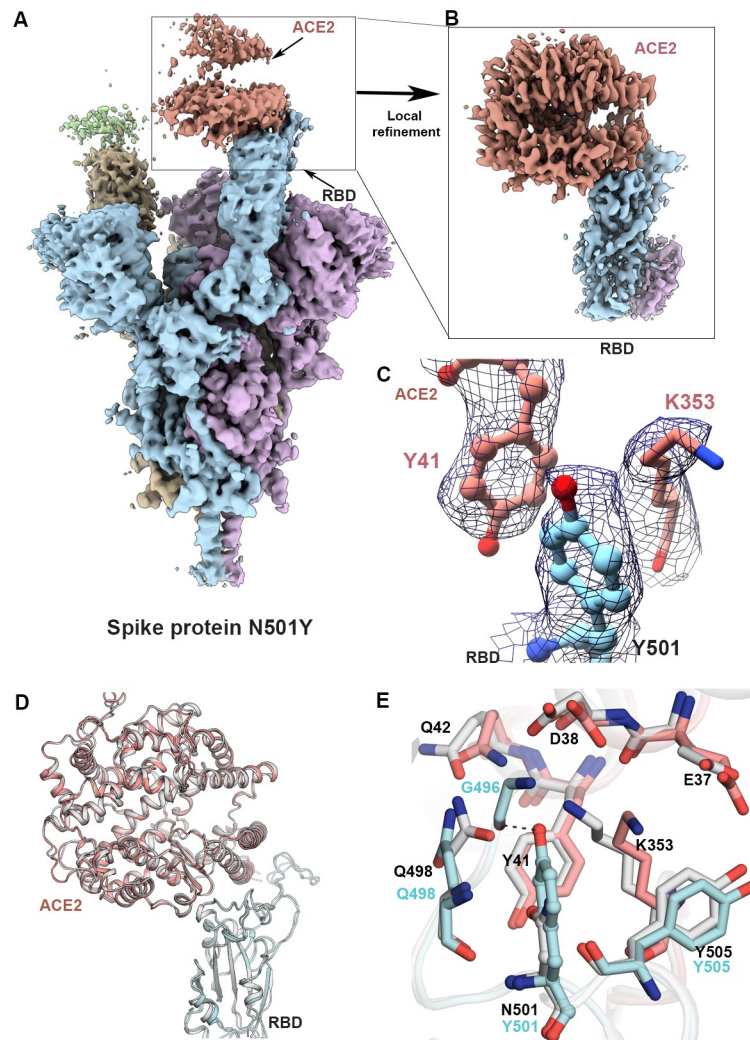
Fig 1. Structure of the SARS-CoV-2 N501Y mutant spike protein ectodomain bound to the ACE2 ectodomain. (A) Density map for the overall complex at the end of global structure refinement. The 3 spike protein protomers are colored in cyan, purple, and yellow, with the density for the strongly and weakly bound ACE2 proteins in pale red and green, respectively. (B) Improved density map at the contact zone between the receptor binding domain (RBD) and the strongly bound ACE2 protein ectodomain. (C) Visualization of density at the contact zone for Y501 in the RBD and residues Y41 and K353 in ACE2. (D). Ribbon diagram with superposition of the unmutated and N501Y RBD–ACE2 complex (PDB ID 7KMB). (E) Zoomed-in view of the interface, showing a superposition of the structures of unmutated and N501Y mutant spike proteins in complex with ACE2. The carbon atoms of residues in the N501Y mutant and ACE2 in our structure are colored in cyan and pale red, respectively, while those in the structure of the complex between unmutated spike protein and ACE2 are in light gray.

potency of IgG ab1. To understand the effects of these antibodies at a structural level, we next determined cryo-EM structures of the complexes formed by V_H ab8 (variable domain of the bivalent fusion construct V_H FC Ab8) and Fab ab1 (the antigen binding fragment of IgG ab1) with the N501Y mutant spike protein ectodomain.

Neutralizing antibodies bind N501Y spikes in different conformational states

Cryo-EM structural analysis of the complex formed between V_H ab8 and the N501Y spike protein ectodomain shows a single dominant conformation with 2 V_H ab8 fragments bound to
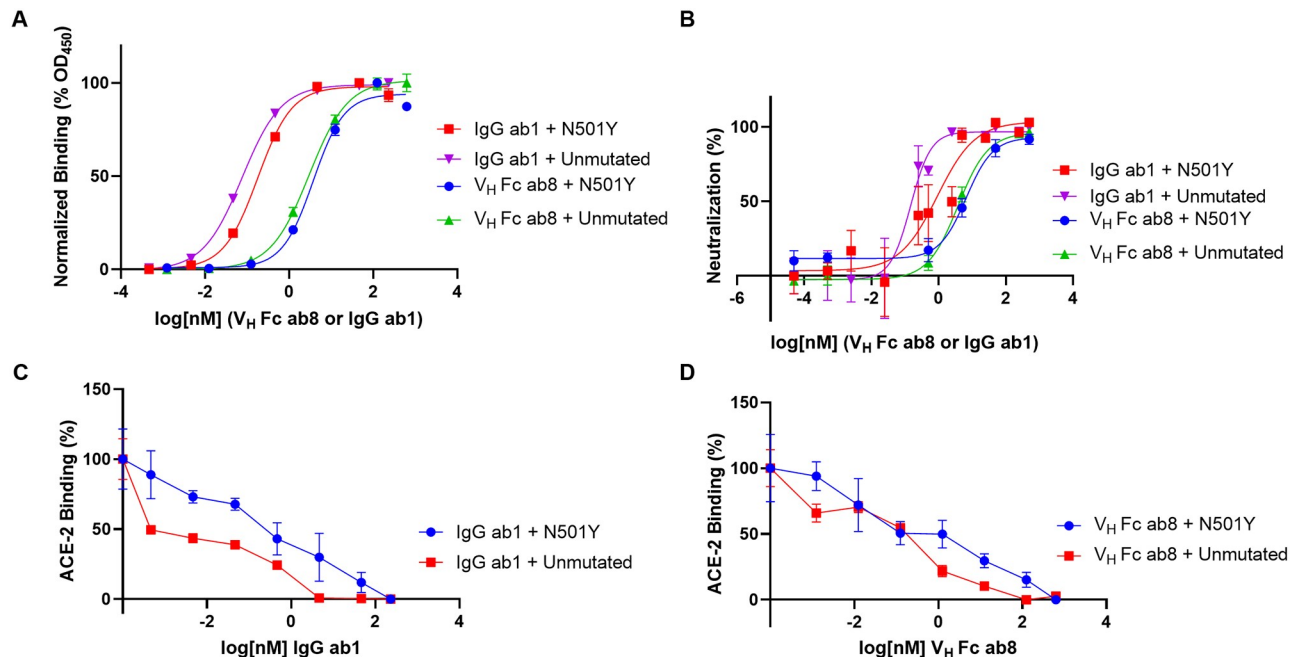
Fig 2. Analysis of V_H Fc ab8 and IgG ab1 interactions with N501Y and unmutated spike. (A) ELISA analysis of antibody interactions with either N501Y or unmutated spike ectodomain. (B) N501Y or unmutated SARS-CoV-2 S pseudotyped virus neutralization by either V_H Fc ab8 or IgG ab1. (C and D) ELISA analysis of N501Y or unmutated SARS-CoV-2 spike ectodomain binding by soluble ACE2-mFc in the presence of serial dilutions of either (C) IgG ab1 or (D) V_H Fc ab8. ELISA experiments were done at least in duplicate while neutralization experiments were performed twice at least in duplicate, and the average values are shown. Error bars denote the standard error of the mean (SEM).

https://doi.org/10.1371/journal.pbio.3001237.g002

RBDs in the down conformation and weak density for the other RBD, which is flexible and primarily in the up position (Fig 3A; S7 Fig). The global average resolution of the map is approximately 2.8 Å, with lower local resolution in the RBD regions, but local refinement yields maps of the V_H ab8–RBD interface at a resolution of approximately 3 Å (Fig 3B; S7 Fig). Cryo-EM density maps unambiguously show the location of residue 501 in the N501Y mutant spike protein ectodomains (Fig 3C). The interface between the RBD and V_H ab8 is well defined, with key interactions at the interface mediated by residues in the stretch between V483 and S494, along with a few other interactions contributed by noncontiguous RBD residues (Fig 3D and 3E). Residue 501 of the spike protein RBD is at the periphery of the footprint of V_H ab8 and shows no evidence of interactions with the antibody. The presence of the mutation thus appears not to influence interactions between the RBD and V_H ab8.

Similar cryo-EM analyses of the complex between the mutated spike protein and Fab ab1 show that in contrast to the V_H ab8 complex, Fab ab1 binding involves either 2 or 3 RBDs, all being in the up position (Fig 4A and 4B; S8 Fig). Local refinement of the RBD–Fab ab1 interface improves the resolution to approximately 3 Å, enabling unambiguous placement of Y501 as well as the residues involved in the contact between the RBD and Fab ab1 (Fig 4C and 4D; S8 Fig). Residue 501 is at the periphery of the Fab ab1 footprint, with Ser 30 of Fab ab1 in a position to interact with this residue (Fig 4E and 4F). The N501Y mutation would thus be expected to have a small effect on the antibody binding epitope. Together, the cryo-EM structures are fully consistent with the studies presented in Fig 2 that show a small but significant effect of the N501Y mutation on Fab ab1 binding and neutralization, but with no measurable effects on V_H ab8 binding or neutralization.
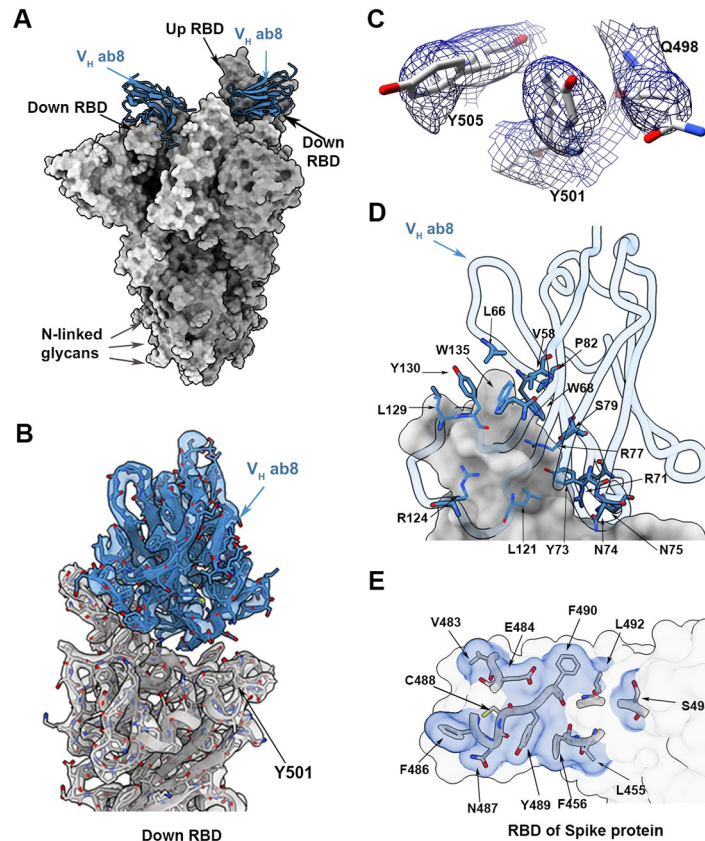
Fig 3. Structure of V$_H$ ab8 bound to the N501Y mutant spike protein trimer. (A) Atomic model for the structure of the complex of V$_H$ ab8 (blue) with the N501Y mutant spike protein ectodomain (gray). The structure has 2 receptor binding domains (RBDs) in the down position with well-resolved densities for the bound V$_H$ ab8. The third RBD is in the up position. (B) Cryo-electron microscopy density map after local refinement with fitted coordinates for the contact zone between the RBD and V$_H$ ab8. (C) Density map in the region near 501 for the N501Y mutant spike protein ectodomain showing density for residues Q498, Y501, and Y505. (D and E) Close-up views of the contact zone between the RBD region and ACE2 highlighting residues involved.

Discussion

Comparison of the structures reported here with those reported for the ACE2–RBD complex from earlier X-ray crystallography and cryo-EM studies enable visualization of the similarities and differences in the modes of binding (Fig 5). There are several regions such as the portion of the epitope in the vicinity of residue F486 that are shared across ACE2 and the 2 antibodies (Fig 5A–5C). However, there are marked differences near residue 501, which is completely within the ACE2 footprint, at the very edge of the ab1 footprint, and well outside the ab8 footprint (Fig 5D–5G). ACE2 binding has been observed only to RBDs in the up position, likely because of steric constraints in accommodating ACE2 in the down conformation. However, the stoichiometry of ACE2 binding to the trimeric spike can be variable. Negative stain experiments show that populations of spike proteins with 1, 2, or 3 ACE2 receptors bound are obtained (S6 Fig), and consistent with the binding studies, we find that a higher number of ACE2 receptors bind N501Y spikes as compared to unmutated spikes when the incubation is carried out under similar conditions. In cryo-EM experiments, Fab ab1 also binds the RBD in only the up position (Fig 4A and 4B), but in contrast, the much smaller V$_H$ ab8 fragment binds the RBD in both up and down positions (Fig 3A). Despite these differences, and the fact that
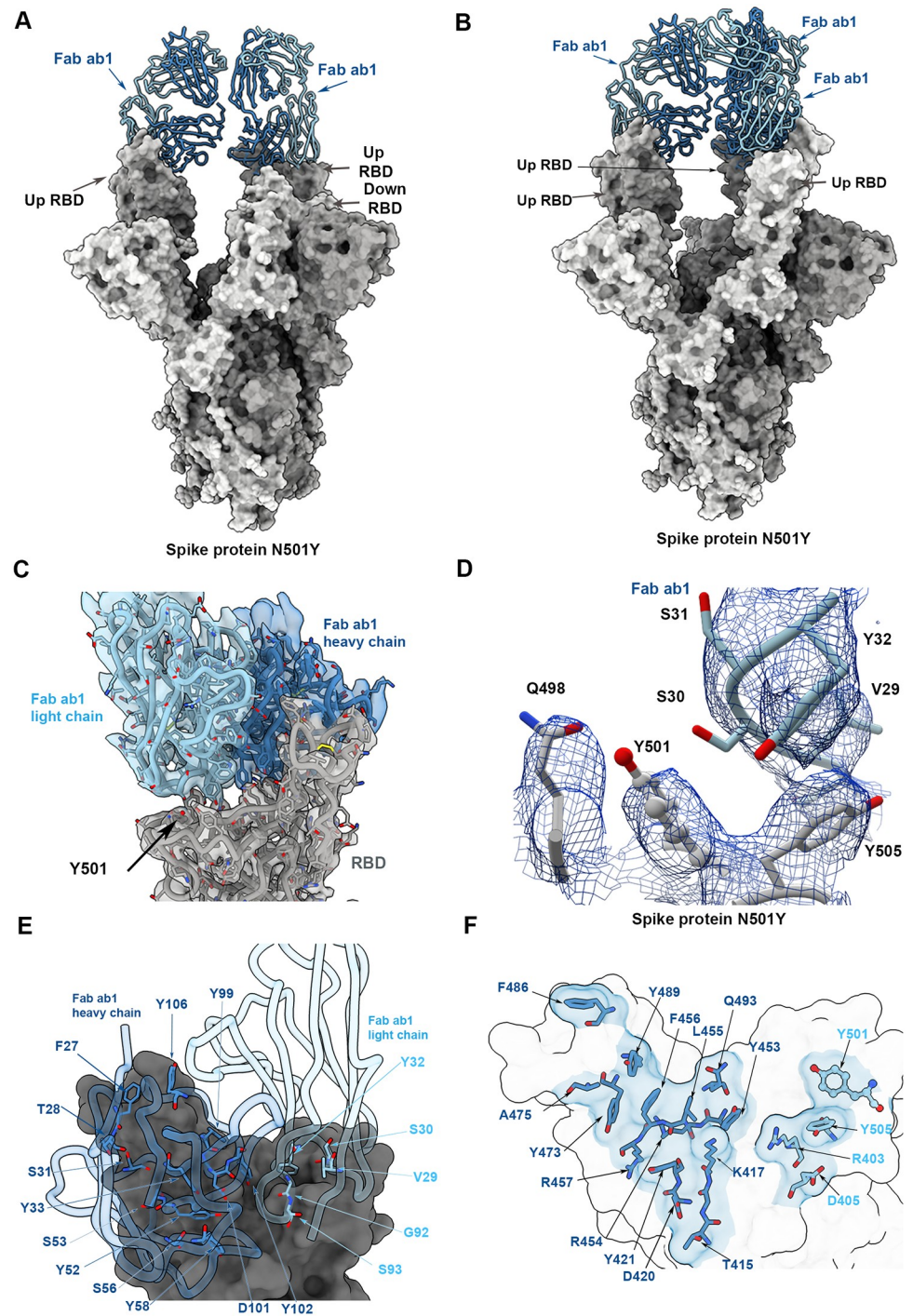
Fig 4. Structure of Fab ab1 bound to the N501Y mutant spike protein trimer. (A and B) Atomic models for the 2 predominant conformations of the spike protein (gray) observed with Fab ab1 (blue) bound to either 2 (A) or 3 (B) receptor binding domains (RBDs) in the up position. (C) Cryo-electron microscopy density map after local refinement with fitted coordinates for the contact zone between the RBD and Fab ab1. (D) Density map in the region near 501 for the N501Y mutant spike protein ectodomain showing density for residues Q498, Y501, and Y505 in the spike protein and a loop in Fab ab1 that includes S30, the residue closest to Y501. (E and F) Close-up views of the contact zone between the RBD region and ACE2 highlighting residues involved.
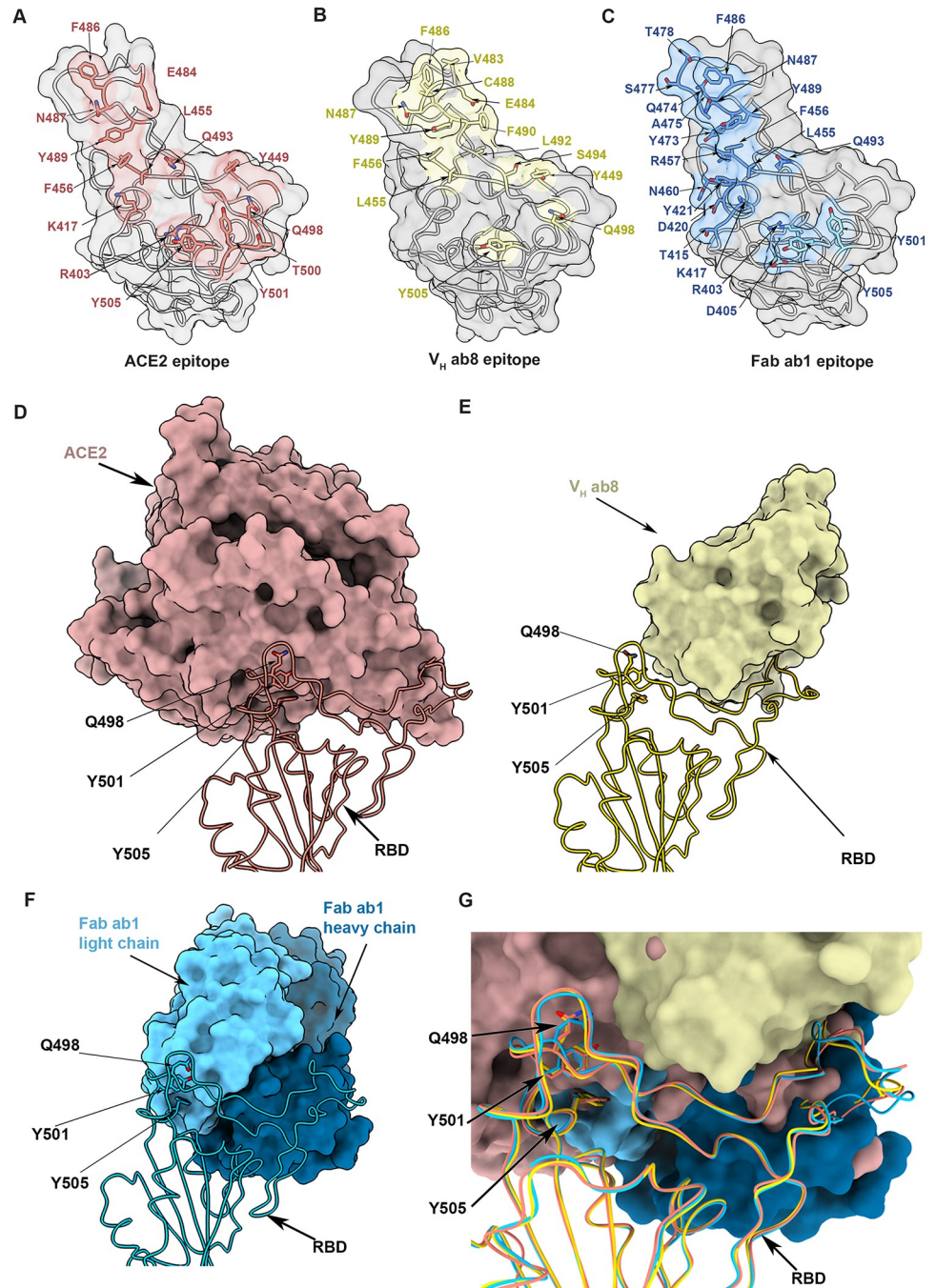
Fig 5. Comparison of the structures of complexes formed by the spike protein ectodomain with the ACE2 ectodomain, V$_H$ ab8, and Fab ab1. (A–C) Open-face views of the receptor binding domain (RBD) from the vantage point of ACE2 (A), V$_H$ ab8 (B), and Fab ab1 (C), with the residues involved in contact shaded in red, yellow, and blue, respectively. (D–F) Space-filling model view of ACE2 (D), V$_H$ ab8 (E), and Fab ab1 (F) in contact with the RBD (structure shown in ribbon format). (G) Superposition of the structures of the complex of the RBD with ACE2, V$_H$ ab8, and Fab ab1 to show their relative footprints on the RBD surface.

https://doi.org/10.1371/journal.pbio.3001237.g005

ACE2, V_H ab8, and Fab ab1 each have distinctive directions of approach in their contact with the RBD, there is a good match in the RBD binding footprint between V_H ab8, Fab ab1, and ACE2 (Fig 5A–5C), accounting for the potent neutralization by the V_H Fc ab8 and IgG1 ab1 antibodies (Fig 5D–5G). The location of residue 501 at the outer edge of the contact zone for the Fab ab1 complex and outside the zone of contact for V_H ab8 complex provides a structural rationale for the findings we describe here on the differential effects of the N501Y mutation on binding and neutralization by these 2 antibodies (Fig 5).

Our studies with the N501Y mutant are consistent with the expectation that the rapid spread of the UK variant of SARS-CoV-2 is likely due to the virus being more infectious. While there can be multiple origins for the increased infectivity, our biochemical studies suggest that the N501Y mutation results in increased ACE2 binding efficiency, a finding that has been reproduced by several recent studies [22–28]. Our structural studies establish the molecular basis underpinning the observed increase in ACE2 binding efficiency conferred by the N501Y mutation. Competition assays with a strongly neutralizing antibody show that it competes for binding with the spike trimer–ACE2 interaction in a concentration-dependent manner. Our results suggest that despite the higher infectivity of SARS-CoV-2 viruses carrying the N501Y mutation, the availability of the extended epitope surface on the RBD enables effective neutralization by V_H ab8 and Fab ab1. The footprints of these antibodies are comparable to those of other antibodies recently described (S2 Table) [29–32], suggesting that at least some antibodies elicited by immunization with vaccines that are currently in production may also retain the ability to neutralize the N501Y mutant. With the continued spread of SARS-CoV-2, it appears likely that further mutations that enhance viral fitness will emerge. Cryo-EM methods to rapidly identify the footprints of antibodies that are generated by current and future generations of vaccines could thus add a critical tool to the arsenal of efforts to prevent and treat COVID-19.

Materials and methods

Cloning, expression, and purification of recombinant spike protein constructs

The wild-type SARS-CoV-2 S HexaPro expression plasmid was a gift from Jason McLellan [7] and was obtained from Addgene (plasmid #154754; http://n2t.net/addgene:154754; RRID: Addgene_154754). The N501Y mutation was introduced by site-directed mutagenesis (Q5 Site-Directed Mutagenesis Kit, New England Biolabs). Successful subcloning and mutation were confirmed by Sanger sequencing (Genewiz). Expi293F cells (Thermo Fisher) were grown in suspension culture using Expi293 Expression Medium (Thermo Fisher) at 37˚C and 8% CO_2. Cells were transiently transfected at a density of 3×10^6 cells/ml using linear polyethylenimine (Polysciences). Twenty-four hours following transfection, the medium was supplemented with 2.2 mM valproic acid, and expression carried out for 5 d at 37˚C and 8% CO_2. The supernatant was harvested by centrifugation and filtered through a 0.22-μm filter before loading it onto a 5-ml HisTrap excel column (Cytiva). The column was washed with 20 column volumes (CVs) of wash buffer (20 mM Tris [pH 8.0], 500 mM NaCl), followed by 5 CVs of wash buffer supplemented with 20 mM imidazole. The protein was eluted with elution buffer (20 mM Tris [pH 8.0], 500 mM NaCl, 500 mM imidazole). Elution fractions containing the protein were pooled and concentrated (Amicon Ultra 100-kDa cutoff, Millipore Sigma) for gel filtration (GF). GF was conducted using a Superose 6 10/300 GL column (Cytiva) pre-equilibrated with GF buffer (20 mM Tris [pH 8.0], 150 mM NaCl). Peak fractions corresponding to soluble protein were pooled and concentrated to 4.5–5.5 mg/ml (Amicon Ultra 100-kDa

cutoff, Millipore Sigma). Protein purity was estimated as >95% by SDS-PAGE, and protein concentration was measured spectrophotometrically (NanoPhotometer N60, Implen).

Negative stain sample preparation and data collection

For negative stain, purified S protein (0.05 mg/ml) was mixed with soluble ACE2 (0.05 mg/ml) and incubated on ice for 15 min. For the competition experiment, the S protein (0.05 mg/ml) was first incubated on ice with V_H ab8 (0.02 mg/ml) for 30 min, followed by addition of ACE2 (0.05 mg/ml) for another 30 min. Grids (copper 200 or 300 mesh coated with continuous ultra-thin carbon) were plasma cleaned using an H_2/O_2 gas mixture for 15 s in a Solarus II Plasma Cleaner (Gatan) or 10 s in a PELCO easiGlow Glow Discharge Cleaning System (Ted Pella). The protein mixtures (4.8 µl) were applied to the grid and allowed to adsorb for 30 s before blotting away excess liquid, followed by a brief wash with Milli-Q H_2O. Grids were stained by 3 successive applications of 2% (w/v) uranyl formate (20 s, 20 s, 60 s). Negative stain grids were imaged using a 200-kV Glacios (Thermo Fisher Scientific) transmission electron microscope (TEM) equipped with a Falcon3 camera operated in linear mode. Micrographs were collected using EPU at nominal 92,000× magnification (physical pixel size 1.6 Å) over a defocus range of −2.0 µm to −1.0 µm with a total accumulated dose of 40 e⁻/Å².

Cryo-EM sample preparation and data collection

For cryo-EM, both N501Y and unmutated SARS-CoV-2 spike ectodomain preparations were deposited on grids at a concentration of 2.25 mg/ml. Complexes were prepared by incubating spike ectodomain preparations with either ACE2 (residues 18–615, New England Biolabs), V_H ab8, or Fab ab1 at molar ratios of 1:1.25, 1:9, and 1:8 (spike trimer to binding partner), respectively. Incubations were performed for 20 min on ice prior to centrifugation at 14,000g for 10 min. Grids were plasma cleaned using an H_2/O_2 gas mixture for 15 s in a Solarus II Plasma Cleaner (Gatan) before 1.8 µl of protein suspension was applied to the surface of the grid. Using a Vitrobot Mark IV (Thermo Fisher Scientific), the sample was applied to either Quanti-foil Holey Carbon R1.2/1.3 copper 300 mesh grids (N501Y spike alone and in complex with ACE2) or UltrAuFoil Holey Gold 300 mesh grids (N501Y spike in complex with V_H ab8 or Fab ab1) at a chamber temperature of 10˚C with a relative humidity level of 100%, and then vitrified in liquid ethane after blotting for 12 s with a blot force of −10. All cryo-EM grids were screened using a 200-kV Glacios (Thermo Fisher Scientific) TEM equipped with a Falcon4 direct electron detector followed by high-resolution data collection on a 300-kV Titan Krios G4 (Thermo Fisher Scientific) TEM equipped with a Falcon4 direct electron detector in electron event registration (EER) mode. Movies were collected at 155,000× magnification (physical pixel size 0.5 Å) over a defocus range of −3 µm to −0.5 µm with a total dose of 40 e⁻/Å² using EPU automated acquisition software (Thermo Fisher).

Image processing

In general, all data processing was performed in cryoSPARC v.2.15 or v.3.0.1 [33] unless stated otherwise.

For negative stain data, motion correction and contrast transfer function (CTF) estimation were performed in RELION v.3.1.1 [34]. Particles were picked by crYOLO v.1.7.6 [35] with a general model (ftp://ftp.gwdg.de/pub/misc/sphire/crYOLO-GENERAL-MODELS/gmodel_phosnet_negstain_20190226.h5). After extraction, particles were imported into cryoSPARC and subjected to 2D classification and 3D heterogeneous classification. Final density maps were obtained by 3D homogeneous refinement.

For cryo-EM data, motion correction in patch mode (EER upsampling factor 1, EER number of fractions 40), CTF estimation in patch mode, reference-free particle picking, and particle extraction (extraction box size 640, Fourier crop to box size 320) were performed on-the-fly in cryoSPARC. After preprocessing, particles were subjected to 2D classification and 3D heterogeneous classification. The initial consensus maps were obtained by 3D homogeneous refinement. Then particles were re-extracted with box size 800 and then binned to 400. Final 3D refinement was done with per particle CTF estimation and aberration correction. Local refinements with a soft mask covering a single RBD and its bound V_H ab8 or ACE2 resulted in improvement of the binding interfaces. C3 symmetry expanded particles were used for local refinement of RBD and its bound Fab ab1. Overall resolution and locally refined resolutions were according to the gold-standard Fourier shell correlation (FSC) [36].

Model building and refinement

Coordinates of PDB 6WGJ and 7CH5 were used as initial models to build the V_H ab8 and Fab ab1, respectively. Individual domains of SARS-CoV-2 HexaPro S trimer (PDB ID 6XKL) were docked into cryo-EM density using UCSF Chimera v.1.15 [37]. Initial models were first refined against sharpened locally refined maps, followed by iterative rounds of refinement against consensus map in Coot v.0.9.3 [38] and Phenix v.1.19 [39]. Glycans were added at N-linked glycosylation sites in Coot. Model validation was performed using MolProbity [40]. Figures were prepared using UCSF Chimera, UCSF ChimeraX v.1.1.1 [41], and PyMOL v.2.2 (Schrodinger).

Pseudovirus neutralization assay

SARS-CoV-2 S N501Y plasmid was obtained from SARS-CoV-2 S plasmid (HDM-IDTSpike-fixK) by site-directed mutagenesis (Q5 Site-Directed Mutagenesis Kit, New England Biolabs). SARS-CoV-2 S and SARS-CoV-2 S N501Y pseudotyped retroviral particles were produced in HEK293T cells as described previously [29]. Briefly, a lentiviral system was utilized in combination with plasmids encoding the full-length SARS-CoV-2 spike, along with a transfer plasmid encoding luciferase and GFP as a dual reporter gene. Pseudoviruses were harvested 60 h after transfection, filtered with 0.45-μm PES filters, and frozen. For cell-entry and neutralization assays, HEK293T-ACE2 cells were seeded in 96-well plates at 50,000 cells per well. The next day, pseudovirus preparations normalized for viral capsid p24 levels (Lenti-X GoStix Plus) were incubated with dilutions of the indicated antibodies, ACE2-mFc (SinoBiological), or medium alone for 1 h at 37˚C prior to addition to cells and incubation for 48 h. Cells were then lysed and luciferase activity assessed using the ONE-Glo EX Luciferase Assay System (Promega) according to the manufacturer's specifications. Detection of relative luciferase units was carried out using a Varioskan Lux plate reader (Thermo Fisher). Percent neutralization was calculated relative to signals obtained in the presence of virus alone for each experiment. The IC_{50} values were calculated using a 4-parameter dose–response (sigmoidal) curve in GraphPad Prism (version 9 for Windows, GraphPad Software). This function provides the 95% confidence interval (95% CI) and standard error of the mean (SEM).

Enzyme-linked immunosorbent assay (ELISA)

One hundred microliters of wild-type or N501Y SARS-CoV-2 S protein preparation was coated onto 96-well MaxiSorp plates at 2 μg/ml in PBS overnight at 4˚C. All washing steps were performed 5 times with PBS + 0.05% Tween 20 (PBS-T). After washing, wells were incubated with blocking buffer (PBS-T + 2% BSA) for 1 h at room temperature. After washing, wells were incubated with dilutions of V_H Fc ab8 or ACE2-mFc (SinoBiological) in PBS-T

+ 0.5% BSA buffer for 1 h at room temperature. After washing, wells were incubated with either Goat Anti-Human IgG (Jackson ImmunoResearch) or Goat Anti-Mouse IgG Fc Secondary Antibody, HRP (Invitrogen) at a 1:8,000 dilution in PBS-T + 0.5% BSA buffer for 1 h at room temperature. After washing, the substrate solution (Pierce 1-Step) was used for color development according to the manufacturer's specifications. Optical density at 450 nm was read on a Varioskan Lux plate reader (Thermo Fisher Scientific). For ACE2 competition assays, experiments were conducted as described above with amendments. Serial dilutions of V_H Fc ab8 were incubated for 30 min at room temperature prior to the addition of 2.5 nM ACE2-mFc (SinoBiological). Wells were then further incubated for 45 min at room temperature. After washing, wells were incubated at a 1:8,000 dilution with Goat Anti-Mouse IgG Fc Secondary Antibody, HRP (Invitrogen) in PBS-T + 0.5% BSA buffer for 1 h at room temperature. After washing, the substrate solution (Pierce 1-Step) was used for color development according to the manufacturer's specifications. Optical density at 450 nm was read on a Varioskan Lux plate reader (Thermo Fisher Scientific). For all experiments, controls for antibody–BSA interactions were performed. For competition assays, controls for Goat Anti-Mouse IgG Fc Secondary Antibody recognition of V_H Fc ab8 were performed. The EC_{50} values were calculated using a 4-parameter dose–response (sigmoidal) curve in GraphPad Prism.

Biolayer interferometry (BLI)

The binding kinetics of SARS-CoV-2 trimers and human ACE2 was analyzed with the biolayer interferometer BLItz (ForteBio). Protein-A biosensors (ForteBio, 18–5010) were coated with ACE2-mFc (40 µg/ml) for 2 min and incubated in DPBS (pH = 7.4) to establish baselines. Concentrations of 100 nM, 200 nM, and 400 nM spike trimers were used for association for 2 min followed by dissociation in DPBS for 5 min. The association (k_{on}) and dissociation (k_{off}) rates were derived from the sensorgram fitting and used to calculate the binding equilibrium constant (K_D).

Supporting information

S1 Fig. Purification of N501Y or unmutated (wild-type [wt]) HexaPro ectodomains. (A) Size exclusion chromatography profile of the indicated affinity-purified HexaPro constructs. Fractions pooled for structural and biochemical studies are indicated by gray shading. (B) SDS-PAGE analysis of pooled and concentrated HexaPro constructs.
(TIF)

S2 Fig. Cryo-EM data processing and validation for the N501Y spike protein ectodomains. (A) Representative micrograph. (B) Representative 2D class averages. (C) Cryo-EM data processing workflow. (D) Fourier shell correlation (FSC) between 2 half maps (red) and FSC between the refined map and model (blue). (E) Local resolution estimation. (F) Viewing direction distribution.
(TIF)

S3 Fig. Superposition of the structure of the N501Y spike protein ectodomains (light orange) with the previously published structure of the unmutated construct (blue; PDB ID 6XKL).
(TIF)

S4 Fig. Cryo-EM data processing and validation for the complex between the N501Y spike protein ectodomain and the ACE2 ectodomain. (A) Representative micrograph. (B) Representative 2D class averages. (C) Cryo-EM data processing workflow. (D) Fourier shell correlation (FSC) between 2 half maps (red) and FSC between the refined map and model (blue). (E)

Local resolution estimation of the global map. (F) Viewing direction distribution. (G) FSC between 2 half maps of local refinement (red) and FSC between the locally refined map and model (blue). (H) Local resolution estimation of the locally refined map.
(TIF)

S5 Fig. Analysis of ACE2 interactions with N501Y and unmutated spike. (A) Analysis of cell entry of N501Y or unmutated SARS-CoV-2 S pseudotyped viral particles. N501Y or unmutated SARS-CoV-2 S pseudotyped virus was normalized for p24 levels and incubated with HEK293T-ACE2 cells for 48 h prior to cell lysis and luciferase activity quantification. (RLU: relative luminescent units). (B) Analysis of N501Y or unmutated SARS-CoV-2 S pseudotyped virus neutralization by soluble ACE2-mFC. The IC_{50} of soluble ACE2-mFC neutralization is 0.066 µg/ml (95% CI 0.026–0.17 µg/ml) for unmutated pseudotyped virus, and 0.0074 µg/ml (95% CI < 0.043 µg/ml; lower bound not accurately determined) for N501Y pseudotyped virus. The IC_{50} for wild-type is greater than that for N501Y, as demonstrated by a 1-tailed Welch test ($p = 3 \times 10^{-5}$). (C and D) Biolayer interferometry analysis of immobilized ACE2 binding by increasing concentrations of either N501Y (A) or unmutated (B) spike ectodomain. Shown is the extent of binding as determined by shift in wavelength (nm: nanometers). Biophysical parameters (K_D, k_{on}, k_{off}) are shown as mean ± standard deviation.
(TIF)

S6 Fig. Negative stain electron microscopy reveals different ACE2 occupancies for unmutated and N501Y spikes. (A and B) Representative micrograph selected from the total dataset for the unmutated (A) or N501Y (B) spike ectodomains in complex with ACE2. The concentrations of spike proteins and soluble ACE2 are the same for both unmutated and N501Y preparations. (C and D) 2D class averages corresponding to (C) the unmutated dataset (1,355 images) and (D) the N501Y dataset (1,125 images), covering the same range of stain thickness. (E and F) Processing workflow. (E) For unmutated spikes, 3D classification reveals an occupancy of 2 or fewer RBDs bound for the 2 most populated initial classes (50% and 34% of all particles from 2D classification). (F) For N501Y spikes, the most populated initial class (63%) has 3 RBDs bound. (G and H) Final refinement of (G) unmutated spikes and (H) N501Y spikes. The density corresponding to bound soluble ACE2 is colored in green. The higher occupancy of ACE2 for N501Y spikes reflects a shift in the equilibrium stoichiometry, consistent with the higher affinity of N501Y spikes for ACE2. (I and J) Competition experiments. Spike ectodomains were first incubated with the V_H ab8 antibody fragment, then with soluble ACE2. The density corresponding to bound V_H ab8 is colored in red. The V_H ab8 antibody fragment competes with ACE2 binding, as demonstrated by the reduced ACE2 occupancy in both (I) the unmutated spike (1 RBD bound) and (J) the N501Y spike (2 RBDs bound).
(TIF)

S7 Fig. Cryo-EM data processing and validation for the complex between the N501Y spike protein ectodomain and VH ab8. (A) Representative micrograph. (B) Representative 2D class averages. (C) Cryo-EM data processing workflow. (D) Fourier shell correlation (FSC) between 2 half maps (red) and FSC between the refined map and model (blue). (E) Local resolution estimation of the global map. (F) Viewing direction distribution. (G) FSC between 2 half maps of local refinement (red) and FSC between the locally refined map and model (blue). (H) Local resolution estimation of the locally refined map.
(TIF)

S8 Fig. Cryo-EM data processing and validation for the complex between the N501Y spike protein ectodomain and Fab ab1. (A) Representative micrograph. (B) Representative 2D class averages. (C) Cryo-EM data processing workflow. (D–I) Fourier shell correlation (FSC)

between 2 half maps (red) and between the refined map and model (blue), with local resolution estimation and viewing direction distribution, for class 1 (D–F) and class 2 (G–I). (J) FSC between 2 half maps of local refinement (red) and between the locally refined map and the model (blue). (K) Local resolution estimation of the locally refined map.
(TIF)

S1 Table. Biophysical parameters.
(DOCX)

S2 Table. Spike protein RBD residues that interact with ACE2 and various antibodies.
(DOCX)

S1 Raw Images.
(PDF)

Acknowledgments

Author Contributions

Conceptualization: Xing Zhu, Dhiraj Mannar, Shanti S. Srivastava, Alison M. Berezuk, Jean-Philippe Demers, James W. Saville, Karoline Leopold, Sagar Chittori, Sriram Subramaniam.

Data curation: Alison M. Berezuk, Jean-Philippe Demers, Katharine S. Tuttle.

Formal analysis: Xing Zhu, Dhiraj Mannar, Shanti S. Srivastava, Alison M. Berezuk, Jean-Philippe Demers, James W. Saville, Wei Li, Sagar Chittori, Sriram Subramaniam.

Funding acquisition: Sriram Subramaniam.

Methodology: Xing Zhu, Dhiraj Mannar, Shanti S. Srivastava, Alison M. Berezuk, James W. Saville, Karoline Leopold, Dimiter S. Dimitrov, Katharine S. Tuttle, Steven Zhou, Sagar Chittori, Sriram Subramaniam.

Project administration: Sriram Subramaniam.

Resources: Dimiter S. Dimitrov, Sriram Subramaniam.

Supervision: Sriram Subramaniam.

Validation: Xing Zhu.

Visualization: Xing Zhu, Dhiraj Mannar, Shanti S. Srivastava, Jean-Philippe Demers.

Writing – original draft: Xing Zhu, Dhiraj Mannar, Shanti S. Srivastava, Alison M. Berezuk, Jean-Philippe Demers, James W. Saville, Karoline Leopold, Wei Li, Sagar Chittori, Sriram Subramaniam.

Writing – review & editing: Xing Zhu, Dhiraj Mannar, Shanti S. Srivastava, James W. Saville, Sagar Chittori, Sriram Subramaniam.

References

1. Cai Y, Zhang J, Xiao T, Peng H, Sterling SM, Walsh RM Jr., et al. Distinct conformational states of SARS-CoV-2 spike protein. Science. 2020; 369(6511):1586–92. Epub 2020/07/23. https://doi.org/10.1126/science.abd4251 PMID: 32694201

2. Henderson R, Edwards RJ, Mansouri K, Janowska K, Stalls V, Gobeil SMC, et al. Controlling the SARS-CoV-2 spike glycoprotein conformation. Nat Struct Mol Biol. 2020; 27(10):925–33. Epub 2020/07/24. https://doi.org/10.1038/s41594-020-0479-4 PMID: 32699321

3. Wrapp D, Wang N, Corbett KS, Goldsmith JA, Hsieh CL, Abiona O, et al. Cryo-EM structure of the 2019-nCoV spike in the prefusion conformation. Science. 2020; 367(6483):1260–3. Epub 2020/02/23. https://doi.org/10.1126/science.abb2507 PMID: 32075877

4. Walls AC, Park YJ, Tortorici MA, Wall A, McGuire AT, Veesler D. Structure, Function, and Antigenicity of the SARS-CoV-2 Spike Glycoprotein. Cell. 2020; 181(2):281–92 e6. Epub 2020/03/11. https://doi.org/10.1016/j.cell.2020.02.058 PMID: 32155444

5. Lan J, Ge J, Yu J, Shan S, Zhou H, Fan S, et al. Structure of the SARS-CoV-2 spike receptor-binding domain bound to the ACE2 receptor. Nature. 2020; 581(7807):215–20. Epub 2020/04/01. https://doi.org/10.1038/s41586-020-2180-5 PMID: 32225176

6. Benton DJ, Wrobel AG, Xu P, Roustan C, Martin SR, Rosenthal PB, et al. Receptor binding and priming of the spike protein of SARS-CoV-2 for membrane fusion. Nature. 2020; 588(7837):327–30. Epub 2020/09/18. https://doi.org/10.1038/s41586-020-2772-0 PMID: 32942285

7. Hsieh CL, Goldsmith JA, Schaub JM, DiVenere AM, Kuo HC, Javanmardi K, et al. Structure-based design of prefusion-stabilized SARS-CoV-2 spikes. Science. 2020; 369(6510):1501–5. Epub 2020/07/25. https://doi.org/10.1126/science.abd0826 PMID: 32703906

8. Ke Z, Oton J, Qu K, Cortese M, Zila V, McKeane L, et al. Structures and distributions of SARS-CoV-2 spike proteins on intact virions. Nature. 2020; 588(7838):498–502. Epub 2020/08/18. https://doi.org/10.1038/s41586-020-2665-2 PMID: 32805734

9. McCallum M, Walls AC, Bowen JE, Corti D, Veesler D. Structure-guided covalent stabilization of coronavirus spike glycoprotein trimers in the closed conformation. Nat Struct Mol Biol. 2020; 27(10):942–9. Epub 2020/08/06. https://doi.org/10.1038/s41594-020-0483-8 PMID: 32753755

10. Shang J, Ye G, Shi K, Wan Y, Luo C, Aihara H, et al. Structural basis of receptor recognition by SARS-CoV-2. Nature. 2020; 581(7807):221–4. Epub 2020/04/01. https://doi.org/10.1038/s41586-020-2179-y PMID: 32225175

11. Yao H, Song Y, Chen Y, Wu N, Xu J, Sun C, et al. Molecular Architecture of the SARS-CoV-2 Virus. Cell. 2020; 183(3):730–8 e13. Epub 2020/09/28. https://doi.org/10.1016/j.cell.2020.09.018 PMID: 32979942

12. Zhou T, Tsybovsky Y, Gorman J, Rapp M, Cerutti G, Chuang GY, et al. Cryo-EM Structures of SARS-CoV-2 Spike without and with ACE2 Reveal a pH-Dependent Switch to Mediate Endosomal Positioning of Receptor-Binding Domains. Cell Host Microbe. 2020; 28(6):867–79 e5. Epub 2020/12/04. https://doi.org/10.1016/j.chom.2020.11.004 PMID: 33271067

13. Yan R, Zhang Y, Li Y, Xia L, Guo Y, Zhou Q. Structural basis for the recognition of SARS-CoV-2 by full-length human ACE2. Science. 2020; 367(6485):1444–8. Epub 2020/03/07. https://doi.org/10.1126/science.abb2762 PMID: 32132184

14. Wolrd Health Organization. SARS-CoV-2 Variants. Geneva: World Health Organization; 2020.

15. Lauring AS, Hodcroft EB. Genetic Variants of SARS-CoV-2-What Do They Mean? JAMA. 2021. https://doi.org/10.1001/jama.2020.27124

16. Davies NG, Barnard RC, Jarvis CI, Kucharski AJ, Munday J, Pearson CAB, et al. Estimated transmissibility and severity of novel SARS-CoV-2 Variant of Concern 202012/01 in England. medRxiv. 2020:2020.12.24.20248822. https://doi.org/10.1101/2020.12.24.20248822

17. Gu H, Chen Q, Yang G, He L, Fan H, Deng YQ, et al. Adaptation of SARS-CoV-2 in BALB/c mice for testing vaccine efficacy. Science. 2020; 369(6511):1603–7. Epub 2020/08/01. https://doi.org/10.1126/science.abc4730 PMID: 32732280

18. Starr TN, Greaney AJ, Hilton SK, Ellis D, Crawford KHD, Dingens AS, et al. Deep Mutational Scanning of SARS-CoV-2 Receptor Binding Domain Reveals Constraints on Folding and ACE2 Binding. Cell. 2020; 182(5):1295–310 e20. Epub 2020/08/26. https://doi.org/10.1016/j.cell.2020.08.012 PMID: 32841599

19. Martinez CR, Iverson BL. Rethinking the term "pi-stacking". Chemical Science. 2012; 3(7):2191–201. https://doi.org/10.1039/C2SC20045G

20. Li W, Schafer A, Kulkarni SS, Liu X, Martinez DR, Chen C, et al. High Potency of a Bivalent Human VH Domain in SARS-CoV-2 Animal Models. Cell. 2020; 183(2):429–41 e16. Epub 2020/09/18. https://doi.org/10.1016/j.cell.2020.09.007 PMID: 32941803

21. Li W, Chen C, Drelich A, Martinez DR, Gralinski LE, Sun Z, et al. Rapid identification of a human antibody with high prophylactic and therapeutic efficacy in three animal models of SARS-CoV-2 infection. Proceedings of the National Academy of Sciences. 2020; 117(47):29832–8. https://doi.org/10.1073/pnas.2010197117 PMID: 33139569

22. Wang P, Nair MS, Liu L, Iketani S, Luo Y, Guo Y, et al. Antibody resistance of SARS-CoV-2 variants B.1.351 and B.1.1.7. Nature. 2021. Epub 2021/03/09. https://doi.org/10.1038/s41586-021-03398-2 PMID: 33684923

23. Collier DA, De Marco A, Ferreira I, Meng B, Datir RP, Walls AC, et al. Sensitivity of SARS-CoV-2 B.1.1.7 to mRNA vaccine-elicited antibodies. Nature. 2021. Epub 2021/03/12. https://doi.org/10.1038/s41586-021-03412-7 PMID: 33706364

24. Laffeber C, de Koning K, Kanaar R, Lebbink JH. Experimental evidence for enhanced receptor binding by rapidly spreading SARS-CoV-2 variants. bioRxiv. 2021:2021.02.22.432357. https://doi.org/10.1101/2021.02.22.432357

25. Liu H, Zhang Q, Wei P, Chen Z, Aviszus K, Yang J, et al. The basis of a more contagious 501Y.V1 variant of SARS-COV-2. bioRxiv. 2021:2021.02.02.428884. https://doi.org/10.1101/2021.02.02.428884

26. Tanaka S, Nelson G, Olson A, Buzko O, Higashide W, Shin A, et al. A recombinant 'ACE2 Triple Decoy' that traps and neutralizes SARS-CoV-2 shows enhanced affinity for highly transmissible SARS-CoV-2 variants. bioRxiv. 2021:2021.03.09.434641. https://doi.org/10.1101/2021.03.09.434641

27. Tian F, Tong B, Sun L, Shi S, Zheng B, Wang Z, et al. Mutation N501Y in RBD of Spike Protein Strengthens the Interaction between COVID-19 and its Receptor ACE2. bioRxiv. 2021:2021.02.14.431117. https://doi.org/10.1101/2021.02.14.431117

28. Wang P, Nair MS, Liu L, Iketani S, Luo Y, Guo Y, et al. Increased Resistance of SARS-CoV-2 Variants B.1.351 and B.1.1.7 to Antibody Neutralization. bioRxiv. 2021. Epub 2021/02/04. https://doi.org/10.1101/2021.01.25.428137 PMID: 33532778

29. Du S, Cao Y, Zhu Q, Yu P, Qi F, Wang G, et al. Structurally resolved SARS-CoV-2 antibody shows high efficacy in severely infected hamsters and provides a potent cocktail pairing strategy. Cell. 2020; 183 (4):1013–23. e13. https://doi.org/10.1016/j.cell.2020.09.035 PMID: 32970990

30. Wu NC, Yuan M, Liu H, Lee C-CD, Zhu X, Bangaru S, et al. An alternative binding mode of IGHV3-53 antibodies to the SARS-CoV-2 receptor binding domain. Cell reports. 2020; 33(3):108274. https://doi.org/10.1016/j.celrep.2020.108274 PMID: 33027617

31. Shi R, Shan C, Duan X, Chen Z, Liu P, Song J, et al. A human neutralizing antibody targets the receptor-binding site of SARS-CoV-2. Nature. 2020; 584(7819):120–4. https://doi.org/10.1038/s41586-020-2381-y PMID: 32454512

32. Yuan M, Liu H, Wu NC, Lee C-CD, Zhu X, Zhao F, et al. Structural basis of a shared antibody response to SARS-CoV-2. Science. 2020; 369(6507):1119–23. https://doi.org/10.1126/science.abd2321 PMID: 32661058

33. Punjani A, Rubinstein JL, Fleet DJ, Brubaker MA. cryoSPARC: algorithms for rapid unsupervised cryo-EM structure determination. Nat Methods. 2017; 14(3):290–6. Epub 2017/02/07. https://doi.org/10.1038/nmeth.4169 PMID: 28165473

34. Scheres SH. RELION: implementation of a Bayesian approach to cryo-EM structure determination. J Struct Biol. 2012; 180(3):519–30. Epub 2012/09/25. https://doi.org/10.1016/j.jsb.2012.09.006 PMID: 23000701

35. Wagner T, Merino F, Stabrin M, Moriya T, Antoni C, Apelbaum A, et al. SPHIRE-crYOLO is a fast and accurate fully automated particle picker for cryo-EM. Commun Biol. 2019; 2:218. Epub 2019/06/27. https://doi.org/10.1038/s42003-019-0437-z PMID: 31240256

36. Bell JM, Chen M, Baldwin PR, Ludtke SJ. High resolution single particle refinement in EMAN2.1. Methods. 2016; 100:25–34. Epub 2016/03/05. https://doi.org/10.1016/j.ymeth.2016.02.018 PMID: 26931650

37. Pettersen EF, Goddard TD, Huang CC, Couch GS, Greenblatt DM, Meng EC, et al. UCSF Chimera–a visualization system for exploratory research and analysis. J Comput Chem. 2004; 25(13):1605–12. Epub 2004/07/21. https://doi.org/10.1002/jcc.20084 PMID: 15264254

38. Emsley P, Lohkamp B, Scott WG, Cowtan K. Features and development of Coot. Acta Crystallogr D Biol Crystallogr. 2010; 66(Pt 4):486–501. Epub 2010/04/13. https://doi.org/10.1107/S0907444910007493 PMID: 20383002

39. Afonine PV, Poon BK, Read RJ, Sobolev OV, Terwilliger TC, Urzhumtsev A, et al. Real-space refinement in PHENIX for cryo-EM and crystallography. Acta Crystallogr D Struct Biol. 2018; 74(Pt 6):531–44. Epub 2018/06/07. https://doi.org/10.1107/S2059798318006551 PMID: 29872004

40. Chen VB, Arendall WB 3rd, Headd JJ, Keedy DA, Immormino RM, Kapral GJ, et al. MolProbity: all-atom structure validation for macromolecular crystallography. Acta Crystallogr D Biol Crystallogr. 2010; 66(Pt 1):12–21. Epub 2010/01/09. https://doi.org/10.1107/S0907444909042073 PMID: 20057044

41. Goddard TD, Huang CC, Meng EC, Pettersen EF, Couch GS, Morris JH, et al. UCSF ChimeraX: Meeting modern challenges in visualization and analysis. Protein Sci. 2018; 27(1):14–25. Epub 2017/07/16. https://doi.org/10.1002/pro.3235 PMID: 28710774